

Programming curvature using origami tessellations

Levi H. Dudte¹, Etienne Vouga¹, Tomohiro Tachi² and L. Mahadevan^{1,3,4,5*}

Origami describes rules for creating folded structures from patterns on a flat sheet, but does not prescribe how patterns can be designed to fit target shapes. Here, starting from the simplest periodic origami pattern that yields one-degree-of-freedom collapsible structures—we show that scale-independent elementary geometric constructions and constrained optimization algorithms can be used to determine spatially modulated patterns that yield approximations to given surfaces of constant or varying curvature. Paper models confirm the feasibility of our calculations. We also assess the difficulty of realizing these geometric structures by quantifying the energetic barrier that separates the metastable flat and folded states. Moreover, we characterize the trade-off between the accuracy to which the pattern conforms to the target surface, and the effort associated with creating finer folds. Our approach enables the tailoring of origami patterns to drape complex surfaces independent of absolute scale, as well as the quantification of the energetic and material cost of doing so.

Origami is an art form that probably originated with the invention of paper in China, but was refined in Japan. The ability to create complex origami structures depends on folding thin sheets along creases, a natural consequence of the large-scale separation between the thickness and the size of the sheet. This allows origami patterns to be scaled; the same pattern can be used at an architectural level or at a nanometric level. The richness of the mathematics of origami¹, together with the promise for technology in the context of creating building blocks for foldable or deployable structures and machines², has led to an explosion of interest in the subject. Much of the complexity of the folding patterns arises from the possibilities associated with the basic origami fold—the unit cell associated with a four-coordinated mountain–valley structure that forms the heart of the simplest origami tessellation depicted in Fig. 1a,c. Indeed, tiling the plane with this unit cell yields the eponymous Miura-ori, popularized as a structure for solar sail design³, although the pattern has been known at least since the fifteenth century, for example, in Bronzino's *Portrait of Lucrezia Panciatichi* (circa 1545). It also occurs in many natural settings, including insect wings and leaves^{4,5}, and vertebrate guts⁶, and is the result of the spontaneous wrinkling of soft adherent thin elastic films^{7–9}. Interest in the Miura-ori and allied patterns has recently been rekindled by an interest in mechanical metamaterials^{10–14} on scales that range from the architectural to the microscopic.

Geometry of Miura-ori

The suitability of the Miura-ori for engineering deployable or foldable structures is due to its high degree of symmetry embodied in its periodicity, and four important geometric properties: it can be rigidly folded (that is, it can be continuously and isometrically deformed from its flat, planar state to a folded state); it has only one isometric degree of freedom, with the shape of the entire structure determined by the folding angle of any single crease; it exhibits negative Poisson's ratio (folding the Miura-ori decreases its projected extent in both planar directions); and it is flat-foldable

(that is, when the Miura-ori has been maximally folded along its one degree of freedom, all faces of the pattern are coplanar).

Given the simplicity of the Miura-ori pattern, a natural question is to ask if it has generalizations. In particular, for an arbitrary surface with intrinsic curvature, does there exist a Miura-ori-like tessellation of the plane that, when folded, approximates that surface? If so, can this pattern be made rigidly foldable with one degree of freedom? The ability to even partially solve this inverse problem would open the door to engineering compact, deployable structures of arbitrary complex geometry, while highlighting the importance of obstructions and constraints that arise when working with materials that transform by virtue of their geometric scale separation. We build on our collective understanding of the geometry of Miura-ori¹⁵, mechanics of origami^{10–14}, existing explorations of the link between fold pattern and geometry¹⁶ (Fig. 1b), and previous origami^{17–19} and kirigami^{20–22} surface approximations, to pose the inverse problem of fitting Miura-like origami tessellations to surfaces with intrinsic curvature. We then show that the problem can be solved for generalized cylinders using a direct geometric construction and for arbitrarily curved surfaces using a simple numerical algorithm. Furthermore, we characterize the deployability of generic structures, showing how modifications to the geometry of patterns fitting the same target surface effectively tunes their mechanical bistability. Finally, we demonstrate self-similarity of patterns across resolution scales and quantify a trade-off between accuracy and effort involved in surface approximation with origami tessellations.

Because the periodic Miura-ori pattern tiles the entire plane, we look for generalized origami tessellations, using quadrilateral unit cells that are not necessarily congruent but vary slowly in shape across the tessellation. An embedding of such a pattern in space can be represented as a quadrilateral mesh given by a set of vertices, with edges connecting the vertices and representing the pattern creases, and exactly four faces meeting at each interior vertex. A quadrilateral mesh of regular valence four

¹Paulson School of Engineering and Applied Sciences, Harvard University, Cambridge, Massachusetts 02138, USA. ²Graduate School of Arts and Sciences, University of Tokyo, Tokyo 153-8902, Japan. ³Departments of Physics, and Organismic and Evolutionary Biology, Harvard University, Cambridge, Massachusetts 02138, USA. ⁴Wyss Institute for Bio-Inspired Engineering, Harvard University, Cambridge, Massachusetts 02138, USA. ⁵Kavli Institute for Nanobio Science and Technology, Harvard University, Cambridge, Massachusetts 02138, USA. *e-mail: lm@seas.harvard.edu

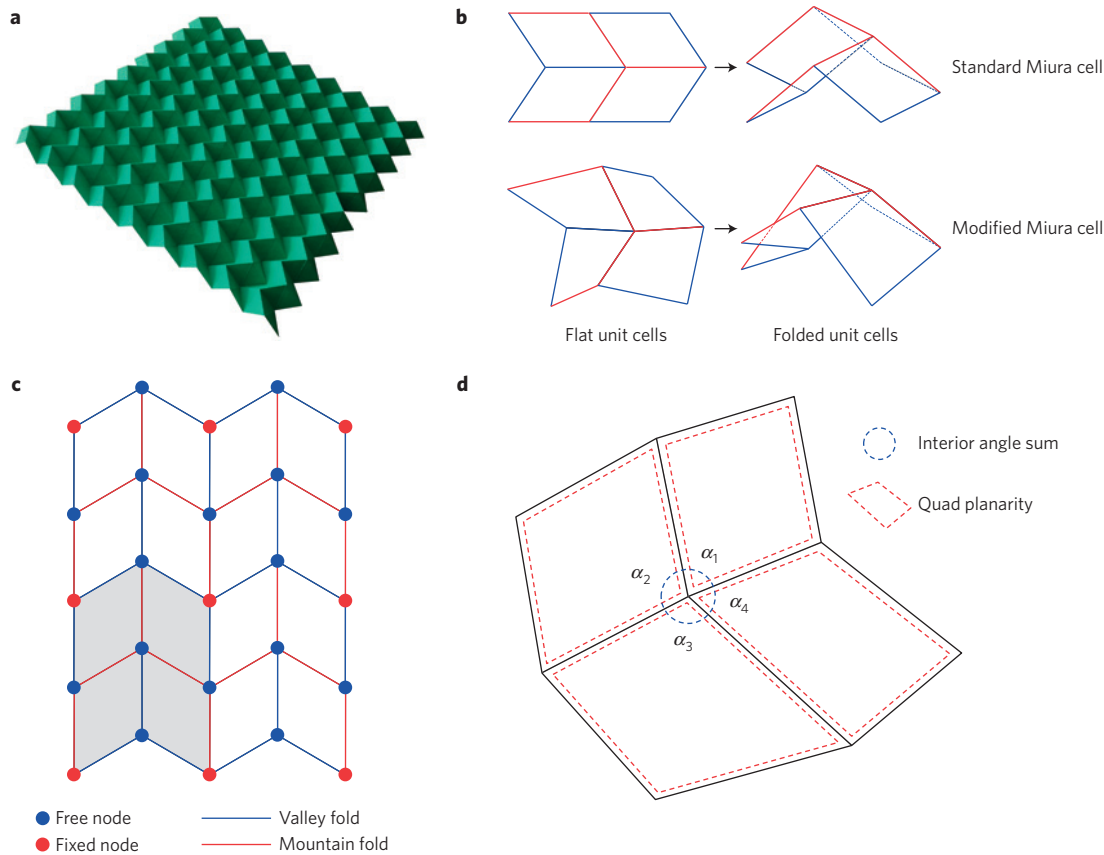


Figure 1 | Geometry of generalized Miura-ori. **a**, Planar periodic Miura-ori. **b**, Standard (top) and modified (bottom) Miura-ori unit cells showing the mountain-valley folds. **c**, Mountain/valley fold orientations and the pattern of fixed/free nodes for the numerical optimization method. Grey shaded area represents one unit cell. **d**, Constraints at nodes and facets. Facet (quad) planarity implies that the volume of the tetrahedron defined by each quad will vanish. Developability requires that $\sum_i^4 \alpha_i = 2\pi$ and local flat-foldability requires $\alpha_1 + \alpha_3 = \alpha_2 + \alpha_4 = \pi$ (Kawasaki's theorem).

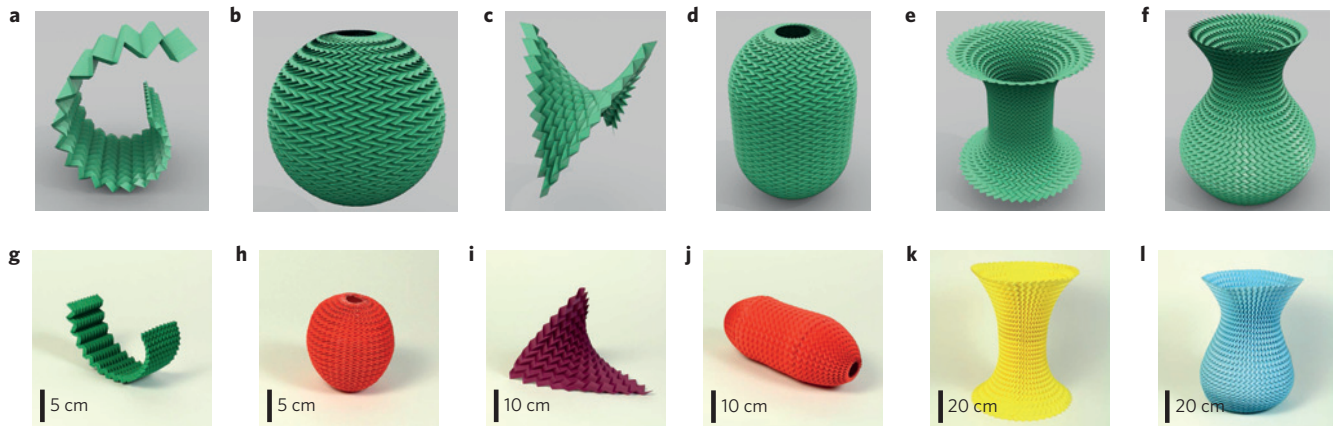


Figure 2 | Optimal calculated origami tessellations and their physical paper analogues. Optimal calculated origami tessellations (**a–f**) and their physical paper analogues (**g–l**). **a,g**, Logarithmic spiral—zero Gauss curvature (generalized cylinder). **b,h**, Sphere—positive Gauss curvature. **c,i**, Hyperbolic paraboloid—negative Gauss curvature. **d,j**, Pill—cylindrical waist with positively curved caps. **e,k**, Candlestick—cylindrical waist with negatively curved caps. **f,l**, Vase—positively curved base with negatively curved neck.

must satisfy two additional constraints to be an embedding of a generalized Miura-ori tessellation: each face must be planar, and the neighbourhood of each vertex must be developable—that is, the interior angles around that vertex must sum to 2π (Fig. 1d).

Inverse origami design

A generalized Miura-ori tessellation is guaranteed to possess some, but not all, of the four geometric properties of the regular Miura-ori

pattern. An arbitrary unit cell has only one degree of freedom, and this local property guarantees that the global Miura-ori pattern, if it is rigid-foldable at all, must have only one degree of freedom. Moreover, because each unit cell must consist of three valley and one mountain crease, or vice versa, it must fold with negative Poisson's ratio. Unfortunately, no local condition is known for whether an origami pattern is flat-foldable; indeed it has been shown²³ that the problem of determining global flat-foldability is

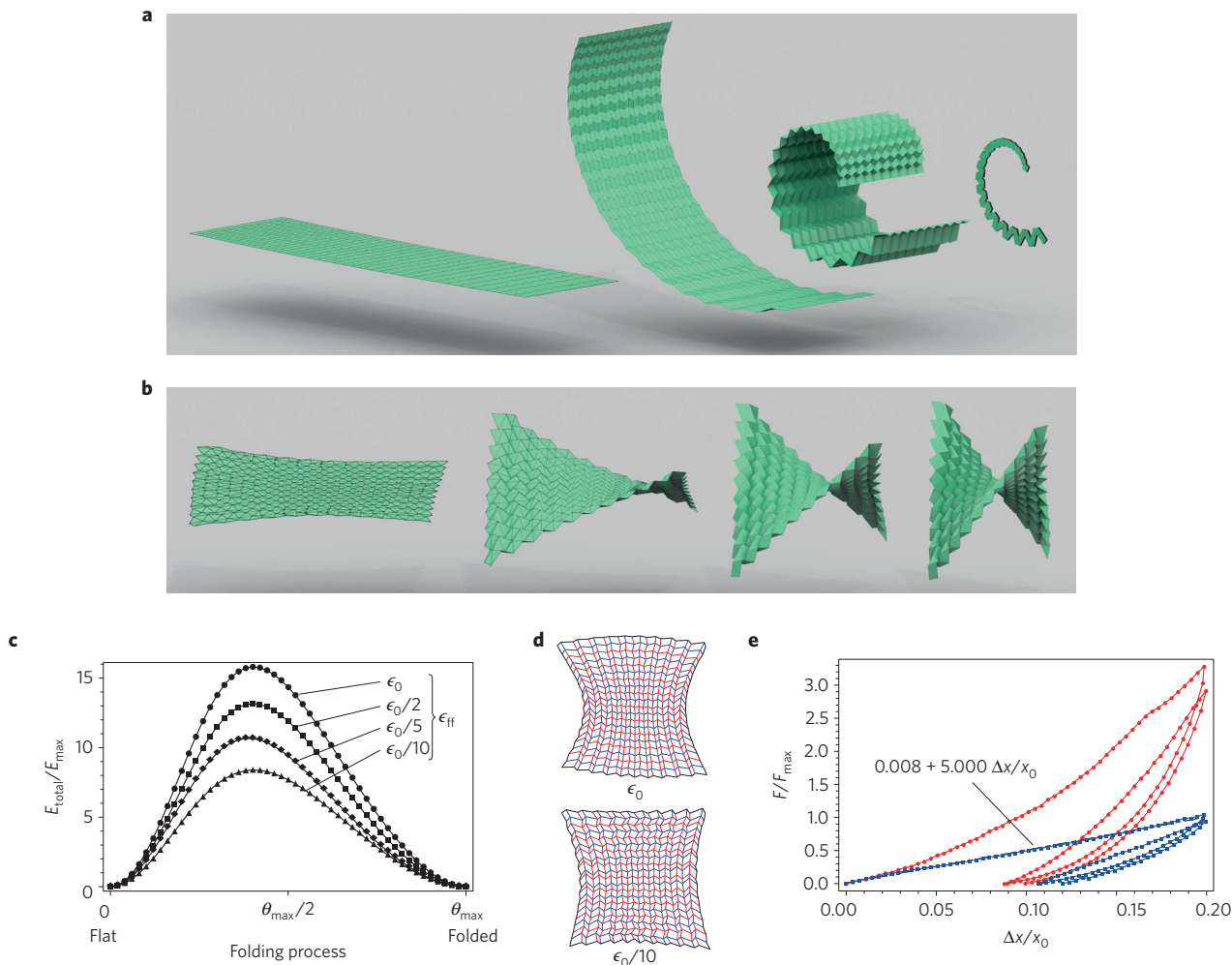


Figure 3 | Foldability. **a**, Generalized cylindrical Miura-ori patterns are rigid-foldable and flat-foldable. The logarithmic spiral here folds rigidly from a flat pattern (left) through the target surface and onto the flat-folded plane (right). **b**, Generalized Miura-ori patterns solved numerically on doubly curved surfaces, however, are not rigid-foldable or flat-foldable. We add an extra edge to each planar quad, thereby allowing bending, to deploy these structures. Shown here is the rigid folding of a triangulated hyperbolic paraboloid pattern from flat (left) to solved (right) states. **c**, Structures that are not rigid-foldable are bistable, with energetic minima at the flat and solved states. For intermediate folding states we minimize the bending of all quads to a non-zero residual strain configuration. Decreasing the flat-foldability residual ϵ_{ff} by an order of magnitude effectively halves the magnitude of the energy barrier. The y axis values represent the total bending energy (E_{total}) normalized by the largest bending energy detected in a single quad during simulation (E_{max}). **d**, Hyperbolic paraboloid patterns with $\epsilon_{\text{ff}} = \epsilon_0 = 1.6 \times 10^{-1}$ (top) and $\epsilon_{\text{ff}} = \epsilon_0/10 = 1.6 \times 10^{-2}$ (bottom) where red/blue indicates mountain/valley assignments. The patterns correspond to the top and bottom energy curves in **c**, respectively (see Supplementary Movie 2). **e**, Force-extension experiments on folded paper hypars corresponding to the patterns in **d** confirm that the larger the residual, the higher the stiffness of the resulting structure (red), and thus the higher the barrier separating these bistable structures ($x_0 = 90$ mm and $F_{\text{max}} = 0.431$ N). The blue values demonstrate the force-extension curve associated with the ‘softer’ structure (**d**, bottom). The first experiment with each structure is different owing to the role of some irreversible deformations; however, after a couple of cycles, the force-extension characteristic settles onto a reproducible curve. The x axis values represent the extension of the origami structure (Δx) normalized by the initial length of the origami structure (x_0).

NP-complete. However, several necessary flat-foldability conditions do exist, of which the two most pertinent are: first, if a generalized Miura-ori tessellation is flat-foldable, each pair of opposite interior angles around each vertex must sum to π (ref. 24; Fig. 1d), and second, if there is a non-trivial generalized Miura-ori embedding (not flat or flat-folded) which satisfies Kawasaki’s theorem, it is globally flat-foldable and rigid-foldable¹⁵. In practice, enforcing a weaker version of Kawasaki’s theorem does improve the degree to which a generalized Miura-ori tessellation is deployable and, in the case where a flat-foldable configuration cannot be found, one can characterize the departure from rigid-foldability by measuring the maximum strain required to deform or snap the bistable tessellation between flat and curved states, a desirable property for stable deployable structures.

These considerations now allow us to formulate the inverse Miura-ori problem: given a smooth surface M in \mathbb{R}^3 of bounded normal curvature, an approximation error ϵ , and a length scale s , does there exist a generalized Miura-ori tessellation that can be isometrically embedded such that the embedding has Hausdorff distance at most ϵ to M ; and also has all edge lengths at least s ? In particular, do there exist such tessellations that satisfy the additional requirement of being flat-foldable? Less formally, we ask here if it is possible to find optimal Miura-ori tessellations that can be used to conform to surfaces with single or double curvature—that is, generalized developables, ellipsoids and saddles, and simple pairwise combinations of these—that might serve as building blocks for more complex sculptures.

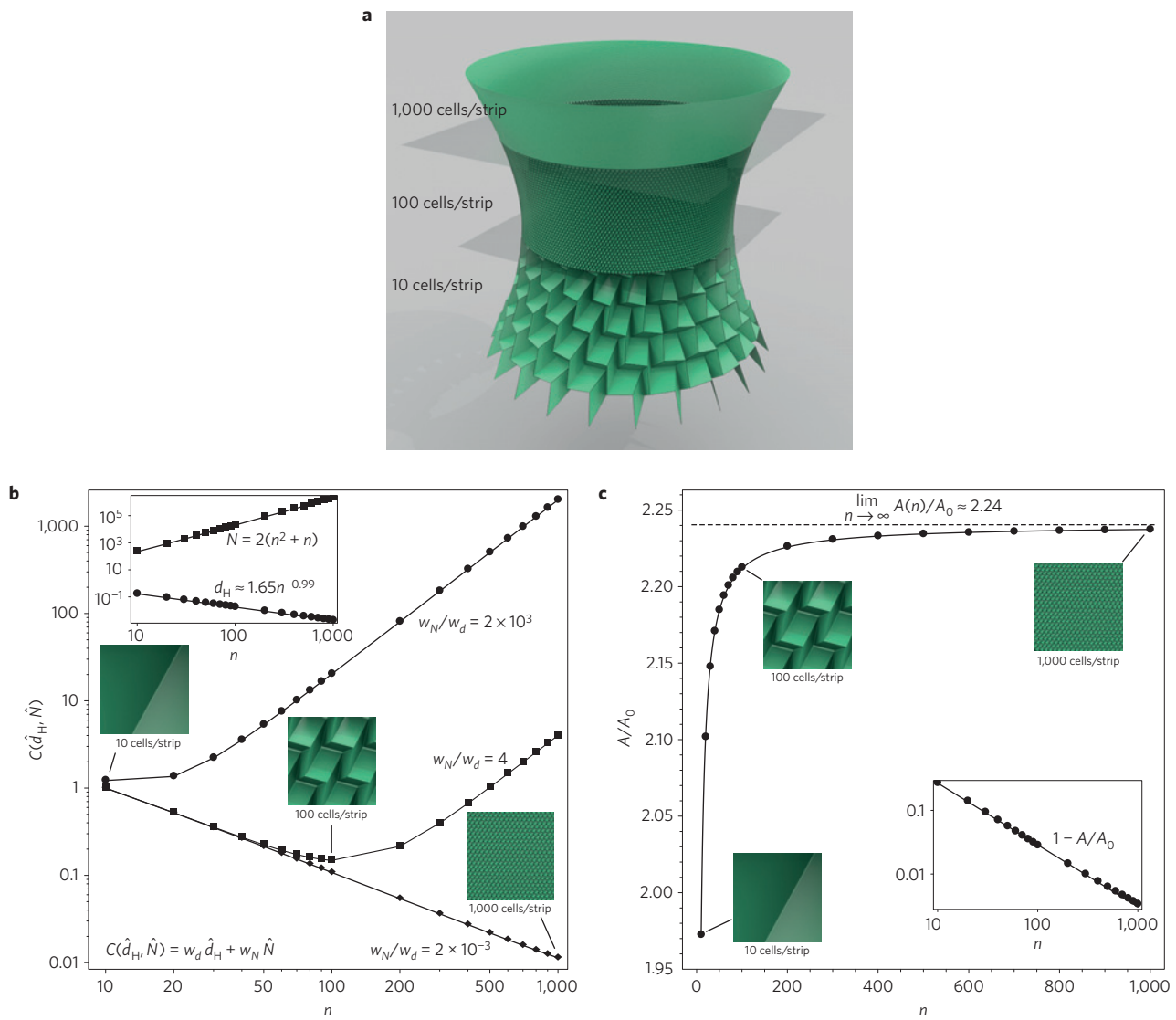


Figure 4 | Accuracy-effort trade-off in origami tessellations. **a**, Three Miura-ori approximations of a hyperboloid, shown in part, differ from each other by a factor of ten in the number of faces (cells) per strip (n). Increasing the density of facets allows us to approach the smooth hyperboloid. **b**, A simple cost function, C , that is the sum of the number of faces normalized by its maximum value (\hat{N}) and the Hausdorff distance normalized by its maximum value (\hat{d}_H) to the smooth hyperboloid as a function of the number of cells (faces) per unit strip (n), shows a clear minimum (see Supplementary Information for details): as the cost of facets (independent of their area) increases, the optimum shifts towards the coarse approximation, whereas as the facets become cheaper, the optimum shifts towards the finer approximation. In the inset, both components of the cost function are shown as a function of the number of faces/strip (n). w_N and w_d are cost weights associated with the number of unit cells (effort) and the Hausdorff distance to the target hyperboloid (accuracy), respectively. **c**, The non-dimensional area of the curved Miura-ori approximation to the hyperboloid (normalized by the area of the smooth hyperboloid) A/A_0 as the number of facets increases approaches a constant greater than unity. In the inset, we see that $(A_0 - A) \sim n^{-1}$, consistent with the fact that the facets are self-similar.

We illustrate the richness of the solution space by starting with a simple analytic construction for generalized cylinders and a numerical algorithm for generic, intrinsically curved surfaces. The generalized cylinder constructions—developable surfaces formed by extruding a planar curve along the perpendicular axis—are guaranteed to be rigid-foldable with one degree of freedom and flat-foldable (see Supplementary Information for details), making them well-suited to applications involving freeform deployable and flat-packed structures (Figs 2a and 3a and Supplementary Movie 1). This is similar to a study published while this work was under review¹⁹, although the numerical approach therein did not recognize the underlying geometric construction and the ensuing rigid-foldability and flat-foldability of this class of surfaces (see Supplementary Information). For more general surfaces M with

intrinsic curvature, we use a numerical optimization algorithm to solve the inverse problem, using the constraints that a quadrilateral mesh approximating M is a generalized Miura-ori if it satisfies a planarity constraint for each face, and a developability constraint at each interior vertex (see Fig. 1d). For a mesh with V vertices and $F \approx V$ faces, there are therefore $3V$ degrees of freedom and only $V + F \approx 2V$ constraints, suggesting that the space of embedded Miura-ori tessellations is very rich; it is therefore plausible that one or more such tessellations that can approximate a given M can be found. Our algorithm allows us to explore this space, constructing tessellations for surfaces of negative, positive, and mixed Gauss curvature. We observe empirically that whereas surfaces of negative Gauss curvature, such as the helicoid and the hyperbolic paraboloid, readily admit generalized Miura-ori

tessellations for a variety of initial guesses for pattern layout, the space of Miura-ori patterns approximating positively curved surfaces such as the sphere is less rich. Indeed, choosing initial layouts that respect the rotational symmetry of the surface is particularly important for rapid convergence in the latter situation, and also yields surfaces of mixed curvature, such as formed by gluing all pairwise combinations of patches—that is, $0/+$, $0/-$, $+/-$ curvature, as shown in Fig. 2a-f. To realize our results physically, we laser-perforated the patterns on sheets of paper and folded them manually, a process that is at present the rate-limiting step in large-scale manufacturability. The results shown in Fig. 2g-l agree well with our calculated shapes.

Energetic and material costs

In contrast with generalized cylinders, solutions to the numerical optimization problem are guaranteed only to be discrete developable, and are not necessarily flat- or rigid-foldable: the tessellation can be embedded without strain so that it approximates M , or so that it is planar, but generally these are isolated states and folding/unfolding the pattern requires snapping through strained configurations (Fig. 3b,c). To characterize the failure of a generalized Miura-ori tessellation to be rigid-foldable, we use a simple physically based numerical simulation: instead of modelling each quadrilateral face of the pattern as rigid and planar, we divide it into a pair of triangles and model it as a thin plate with an elastic hinge (see Supplementary Information for details). Beginning with the folded configuration, we choose one crease in the pattern and incrementally decrease its bending angle from its folded value $\theta = \theta_{\max}$ to its flat value $\theta = 0$. For each intermediate value of the angle, we allow the pattern to relax to static equilibrium; the strain energy of the equilibrium configuration measures the geometric frustration of that intermediate state (Fig. 3c).

To tune this bistability we introduce an inequality constraint in our numerical optimization approach, by replacing Kawasaki's theorem with a tolerance on the residual associated with deviations from flat-foldability given by $|\pi - \alpha_1 - \alpha_3| \leq \epsilon_{\text{ff}} \ll 1$, as shown in Fig. 1. Because flat-foldability implies rigid-foldability for non-trivial configurations¹⁵, decreasing ϵ_{ff} is expected to yield Miura-ori patterns that are closer to rigid-foldable. We test this by considering a Miura-ori tessellation approximating a hyperbolic paraboloid. In Fig. 3c,d, we show that this is indeed the case; reducing the flat-foldability residual by an order of magnitude yields a pattern that approximates the same target surface, but whose energy barrier to folding is half that of the pattern found without the flat-foldability restriction (see Supplementary Movie 2 for a visualization of the energy barriers as a function of the geometry of folding). To confirm this experimentally, we subjected folded paper hypars with two extreme values of the flat-foldable residuals to a simple tensile test. In Fig. 3e, we see that the hypar with the larger residual is stiffer, confirming our theoretical predictions (see Supplementary Information for experimental details).

Finally, we turn to the accuracy of using folded structures to approximate smooth surfaces. Clearly, as the individual folds become finer the resulting structure will conform more closely to the desired target and will require more effort to fabricate. To quantify the trade-off between accuracy and effort, we consider an origami representation of the hyperboloid, shown in Fig. 4a, using three different values for the density of cells (n), each separated by an order of magnitude. A simple cost function associated with the weighted sum of the number of faces (N) and the Hausdorff distance (d_H) to the smooth surface allows us to follow the minimum cost as a function of the relative weight penalizing effort and accuracy (see Supplementary Information for details); as expected, when facets are cheap, one can get high accuracy at low cost, but as they become more expensive, for the same cost, accuracy plummets, as shown in Fig. 4b. Furthermore, as the number of facets increases, the area of

the folded origami tessellation scaled by the true area of the smooth surface it approximates asymptotically approaches a constant, as shown in Fig. 4c.

Outlook

Our study provides an optimization-based procedure to solve the inverse problem of determining generalized Miura-ori tessellations that conform to prescribed surfaces. For generalized cylinders, we have shown that the constructed pattern is rigid-foldable and flat-foldable, and thus can be easily adapted to thick origami²⁵. For doubly curved surfaces, our computational tool allows us to calculate physically realizable tessellations, which we confirm by building paper models. When the Miura-ori tessellations found using our tool are not flat-foldable, a mechanical model of these surfaces allows us to quantify the strains and energetics associated with snap-through as the pattern moves from the flat to folded configuration. Refining the process allows the folded approximant to approach the smooth target surface, which we quantify via a trade-off between accuracy and effort. All together our study opens the way to origamize arbitrary smooth heterogeneously curved surfaces by starting with the simplest origami fold and stitching together an alphabet of generalized Miura-ori tessellations into a flexible design language for engineering shape at any scale.

Methods

Methods and any associated references are available in the online version of the paper.

Received 28 October 2015; accepted 10 December 2015; published online 25 January 2016

References

1. Demaine, E. & O'Rourke, J. *Geometric Folding Algorithms: Linkages, Origami, Polyhedra* (Cambridge Univ. Press, 2011).
2. Lang, R. *Origami Design Secrets* 2nd edn (CRC Press, 2011).
3. Miura, K. *Method of Packaging and Deployment of Large Membranes in Space* Report No. 618 (Institute of Space and Astronautical Science, 1985).
4. Kobayashi, H., Kresling, B. & Vincent, J. The geometry of unfolding tree leaves. *Proc. R. Soc. Lond. B* **265**, 147–154 (1998).
5. Mahadevan, L. & Rica, S. Self-organized origami. *Science* **307**, 1740 (2005).
6. Shyer, A. *et al.* Villification: how the gut gets its villi. *Science* **342**, 212–218 (2013).
7. Bowden, N., Brittain, S., Evans, A. G., Hutchinson, J. & Whitesides, G. Spontaneous formation of ordered structures in thin films of metals supported on an elastomeric polymer. *Nature* **393**, 146–149 (1998).
8. Rizzieri, R., Mahadevan, L., Vaziri, A. & Donald, A. Superficial wrinkles in stretched, drying gelatin films. *Langmuir* **22**, 3622–3626 (2006).
9. Audoly, B. & Boudaoud, A. Buckling of a stiff film bound to a compliant substrate – Part III: Herringbone solutions at large buckling parameter. *J. Mech. Phys. Solids* **56**, 2444–2458 (2008).
10. Wei, Z. Y., Guo, Z. V., Dudte, L., Liang, H. Y. & Mahadevan, L. Geometric mechanics of periodic pleated origami. *Phys. Rev. Lett.* **110**, 215501 (2013).
11. Schenck, M. & Guest, S. D. Geometry of Miura-folded metamaterials. *Proc. Natl Acad. Sci. USA* **110**, 3276–3281 (2013).
12. Silverberg, J. L. *et al.* Using origami design principles to fold reprogrammable mechanical metamaterials. *Science* **345**, 647–650 (2014).
13. Silverberg, J. L. *et al.* Origami structures with a critical transition to bistability arising from hidden degrees of freedom. *Nature Mater.* **14**, 389–393 (2015).
14. Waitukaitis, S., Menaut, R., Chen, B. & van Hecke, M. Origami multistability: from single vertices to metasheets. *Phys. Rev. Lett.* **114**, 055503 (2015).
15. Tachi, T. Hangai prize papers for 2009: generalization of rigid-foldable quadrilateral-mesh origami. *J. IASS* **50**, 173–179 (2009).
16. Gattas, M. & You, Z. Miura-based rigid origami: parametrizations of curved-crease geometries. *J. Mech. Des.* **136**, 121404 (2014).
17. Tachi, T. Origamizing polyhedral surfaces. *IEEE Trans. Vis. Comput. Graphics* **16**, 298–311 (2010).
18. Tachi, T. Freeform origami tessellations by generalizing Resch's patterns. *J. Mech. Des.* **135**, 111006 (2013).

19. Zhou, X., Wang, H. & You, Z. Design of three-dimensional origami structures based on vertex approach. *Proc. R. Soc. A* **471**, 2184–2195 (2015).
20. Castle, T. *et al.* Making the cut: lattice kirigami rules. *Phys. Rev. Lett.* **113**, 245502 (2014).
21. Sussman, D. *et al.* Algorithmic lattice kirigami: a route to pluripotent materials. *Proc. Natl Acad. Sci. USA* **112**, 7449–7453 (2013).
22. Blees, M. K. *et al.* Graphene kirigami. *Nature* **524**, 204–207 (2015).
23. Bern, M. W. & Hayes, B. The complexity of flat origami. *Proc. 7th Annu. (ACM-SIAM) Symp. Discrete Algorithms* 175–183 (1996).
24. Kawasaki, T. *Proc. 1st Int. Meeting Origami Sci. Technol.* (ed. Huzita, H.) 229–237 (1989).
25. Chen, Y., Peng, R. & You, Z. Origami of thick panels. *Science* **349**, 396–400 (2015).

Acknowledgements

We thank the Harvard Microrobotics Lab for help with laser cutting; J. Weaver and O. Ahanotu for help with measuring the stress-strain behaviour of origami hypars; and

the Harvard MRSEC DMR 14-20570, NSF/JSPS EAPSI 2014 (L.H.D.), NSF DMS-1304211 (E.V.), Japan Science and Technology Agency Presto (T.T.) and the MacArthur Foundation (L.M.) for partial financial support.

Author contributions

L.H.D., E.V. and L.M. conceived and designed the research, with later contributions from T.T.; L.H.D. conducted the simulations and built the models; L.H.D., E.V. and L.M. analysed the results and wrote the manuscript.

Additional information

Supplementary information is available in the [online version of the paper](#). Reprints and permissions information is available online at www.nature.com/reprints. Correspondence and requests for materials should be addressed to L.M.

Competing financial interests

The authors declare competing financial interests: details accompany the paper at <http://www.nature.com/naturematerials>. L.H.D., E.V. and L.M. are co-inventors of the surface-fitting algorithm and design method, patent-pending.

Programming curvature using origami tessellations

Levi Dudte, Etienne Vouga, Tomohiro Tachi, L. Mahadevan

Contents

1	Geometry of the Miura-ori	2
2	Constructing Generalized Miura-ori tessellations	3
2.1	Explicit Construction for Generalized Cylinders	3
2.2	Curved Surfaces	5
2.2.1	Initial Positions	7
2.2.2	Fixed Nodes	7
2.2.3	Developability Constraints	8
2.2.4	Flat-Foldability Constraints	8
2.2.5	Special Cases	9
2.2.6	Objective Function	10
2.2.7	Numerical Optimization Approach	10
3	Examples	11
4	Foldability	11
4.1	Simulation Method	13
4.2	Structural Mechanics of Origami	15
4.3	Experimental measurement of Hypar stiffness	16
5	Accuracy vs. Effort: Hyperboloid of a Single Sheet	17
5.1	Base Mesh: Diagonal, Rotationally Symmetric Strip	18
5.2	Examples	19
5.3	Computing the Hausdorff Distance	20
5.4	Accuracy/Effort Trade-Off	22
5.5	Area Convergence	22

1 Geometry of the Miura-ori

An origami tessellation made of unit cells composed of four quadrilaterals, as in the Miura-ori pattern, but whose unit cells are not necessarily congruent but vary in shape across the tessellation, will be termed a *generalized Miura-ori pattern*. An embedding of such a pattern in \mathbb{R}^3 can be represented as a quadrilateral mesh: a set of vertices $p^i \in \mathbb{R}^3$, edges connecting the vertices and representing the Miura-ori creases, and faces, with four faces meeting at each interior vertex. Given an arbitrary quadrilateral mesh of regular valence four, when is it an isometric embedding of some generalized Miura-ori tessellation? Two constraints are evident: each quadrilateral face must be planar, and the neighborhood of each vertex must be *developable*, i.e. the interior angles around that vertex must sum to 2π . It is also easy to see that these conditions are sufficient, in the case that the tessellation is assumed to be topologically trivial.

A quadrilateral mesh that satisfies these conditions is an isometrically embedded generalized Miura-ori tessellation, but what about the four additional properties listed in the introduction?

- One degree of freedom: a unit cell with four planar quads in generic position, i.e. whose four creases have nonzero turning angle, has only one degree of freedom. This local property bounds the possible global isometric deformations: the Miura-ori pattern, if it is rigid-foldable at all, has only one degree one freedom, except in the degenerate case where one of more of its hinges have zero turning angle.
- Negative Poisson’s ratio: this property again can be understood by examining a single unit cell: a rigid-foldable unit cell must consist of three valley and one mountain crease, or vice-versa, and hence folds with negative Poisson’s ratio.
- Rigid-foldability: As demonstrated by Tachi [1], finding a non-trivial flat-foldable configuration of a structure (neither flat nor flat-folded) guarantees rigid-foldability with a single DOF. In the case where a flat-foldable configuration (and therefore rigid-foldable) cannot be found, one can instead characterize the residual strain required when folding the tessellation from its flat to its embedded state by subdividing quads into triangle pairs (effectively increasing the DOFs) and rigid-folding this modified pattern.
- Flat-foldability: Unfortunately, no sufficient local condition exists for whether a flat origami pattern is globally flat-foldable, and it is known [3] that the problem is NP-complete. However several necessary local conditions do exist, the most salient of which is Kawasaki’s Theorem [4]; applied to the generalized Miura-ori pattern, it states that if the pattern is flat-foldable, each pair of opposite interior angles around each vertex must sum to π . We shall see in Section 4 that in practice, enforcing a loose version Kawasaki’s theorem improves the mechanical performance of the origami

tessellation during folding.

2 Constructing Generalized Miura-ori tessellations

The inverse Miura-ori design problem can now be formulated: given a smooth surface M in \mathbb{R}^3 with boundary that is homeomorphic the disk, an approximation error ϵ , and a length scale s , does there exist a generalized Miura-ori tessellation that a) can be isometrically embedded such that the embedding has Hausdorff distance at most ϵ to M ; b) has all edge lengths at least s ? Does there exist such tessellations that satisfy the additional requirement of being flat-foldable?

Experiments suggest that the Gaussian curvature of M significantly influences the difficulty of this inverse problem. Developable surfaces and surfaces with negative Gaussian curvature both readily admit approximations by generalized Miura-ori tessellations; the numerical optimization presented below can also find Miura-ori approximations of positively-curved surfaces, but the space of such tessellations appears to less rich.

2.1 Explicit Construction for Generalized Cylinders

The simplest case is that of generalized cylinders – developable surfaces formed by extruding a planar curve along the perpendicular axis. Therefore, we first give a constructions for approximating generalized cylinders – surfaces $r(s, t) = \gamma(s) + t\hat{z}$ for a plane curve γ – by flat-foldable generalized Miura-ori tessellations. We begin by approximating $\gamma(s)$ by a piecewise-linear discrete curve passing through N nodes Γ_i , and choose a set of N control points P_i on one side of the curve for the Miura-ori structure to pass through. To understand this, consider a strip of paper with uniform width, shown in blue, and rigidly align the left boundary of the strip with the line passing through Γ_1 and P_1 (see Fig. S.1a). Now draw a line (shown dashed) to the next node Γ_2 and fold the strip along the bisector of $\Gamma_1 P_1$ and $P_1 \Gamma_2$, shown in red. Continuing this process along all N nodes and control points, with each crease edge given by a bisection yields a construction that has $2N$ free parameters – the position each control point. Then the pattern can be optimized for ϵ or other design goals such as regularity of the quadrilaterals, etc. and indeed it can be shown that several such strips can be glued together into a generalized Miura-ori pattern approximating a generalized cylinder of any curvature, such as extruded spirals or sine waves that are completely flat-foldable (see Movie1).

Call the previous construction a *Miura-ori strip*. Given a extrusion parameter T , several copies of a Miura-ori strip can be glued into a generalized Miura-ori tessellation approximating the generalized cylinder $r(s, t) = \gamma(s) + t\hat{z}$. Take strip j and displace the right side of the strip by T in the \hat{z} direction, if j is odd, or the left side, if j is even (see Fig.

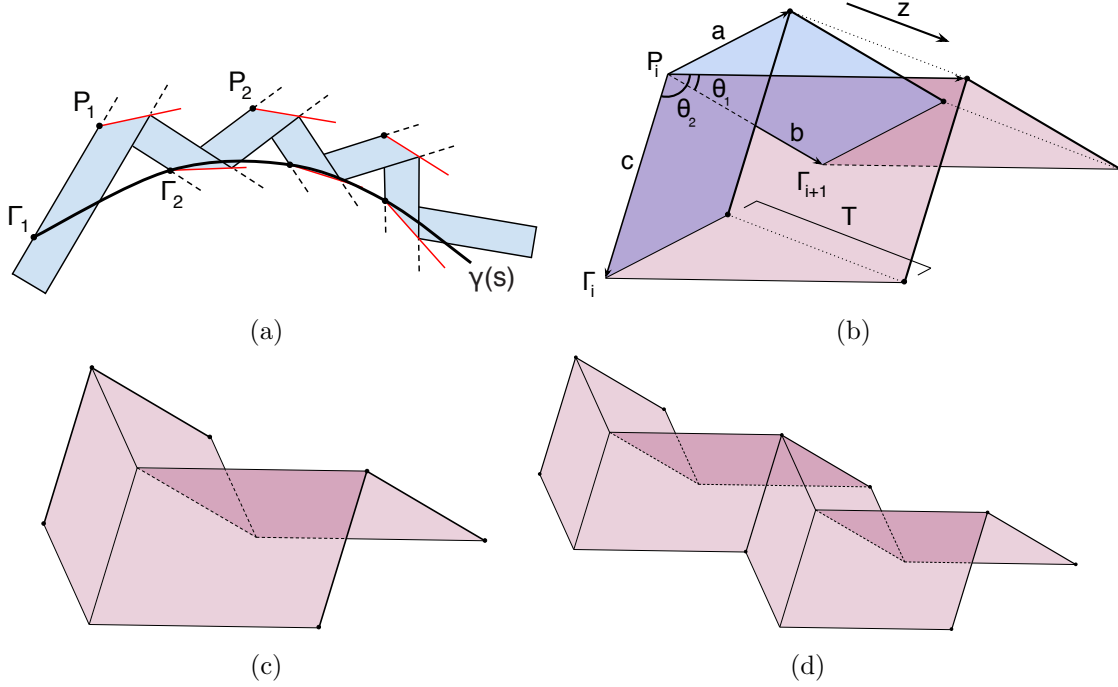


Figure S.1: **Geometric construction** **(a)** In-plane strip construction: choose Γ_i to discretize a smooth curve $\gamma(s)$, choose control points P_i , beginning at Γ_1 wrap a strip of uniform width (blue) back and forth between the discretization and control points, reflecting over bisectors (red) of the lines through Γ_i , P_i and P_i , Γ_{i+1} . **(b)** Extrude all points on one side of the strip by T . **(c)** Mirror the strip over the construction plane to produce a single column of Miura-ori cells. **(d)** Translate and glue copies of the column to create a generalized Miura-ori cylinder.

S.1d), then translate the entire strip rigidly in the \hat{z} direction by jT to complete a new column of Miura-ori cells. It is clear that the strips align as a quadrilateral mesh, that they approximate r , and that the faces of the mesh are planar. It remains to be shown that this mesh is developable at the vertices.

Consider θ_1 and θ_2 , the interior angles of two consecutive quads in the strip construction, in Fig. S.1b. Because this strip will be mirrored to form a column of Miura-ori cells, developability requires that $\theta_1 + \theta_2 = \pi$. Denoting by a, b, c the lengths of the edges marked in Fig. S.1b, we can lay out a coordinate system with $a(T) = (A, 0, T)$, $b = (B_1, B_2, 0)$ and $c = (C_1, C_2, 0)$ for some A, B_i, C_i , and

$$\cos \theta_1(T) = \frac{AB_1}{\sqrt{A^2 + T^2} \sqrt{B_1^2 + B_2^2}}$$

$$\cos \theta_2(T) = \frac{AC_1}{\sqrt{A^2 + T^2} \sqrt{C_1^2 + C_2^2}}$$

Setting $K(T) = \frac{A}{\sqrt{A^2 + T^2}}$ we have

$$\cos \theta_1(T) + \cos \theta_2(T) = K(T)(\cos \theta_1(0) + \cos \theta_2(0)) = 0$$

since by construction $\theta_1(0) + \theta_2(0) = \pi$ and so $\cos \theta_1(0) + \cos \theta_2(0) = 0$. Therefore $\theta_1(T) + \theta_2(T) = \pi$ and the tessellation is developable for any T .

Additionally, when consecutive strips of the tessellation are mirrored, the sum of opposite interior angles about any vertex is also $\theta_1(T) + \theta_2(T)$, and so the construction yields a tessellation that satisfies Kawasaki's condition (locally flat-foldable) at every node. The tessellation is trivially globally flat-foldable and rigid-foldable, which can be seen by observing that in any folded state the width of each strip in the z direction is constant and all strips are identical up to rigid translation and reflection (see Fig. S.2).

While our work was under review, we were made aware of a paper that focuses on a small subset of the problems treated here, namely that finding patterns that fit interstitially between two generalized cylindrical surfaces, and by choosing control points P to fit a second generalized cylindrical surface [2]. Our method provides a simple geometric approach for the surface types solved for numerically in [2]. Our construction recovers this application, but also explicitly guarantees flat- and rigid-foldability, two properties left unproven by the authors of [2]. Because our method guarantees these properties by construction, we implement a simple layout algorithm which directly computes intermediate folding states of the Miura strip using spherical trigonometric relationships between fold and interior angles [5], instead of relying on a numerical simulation to determine these states as in [2].

2.2 Curved Surfaces

For surfaces with intrinsic curvature, to our knowledge no explicit generalized Miura-ori construction exists; we propose a numerical optimization algorithm to solve for a tessellation in this setting. Let M be the target surface that is to be approximated, and parameterize the embedded generalized Miura-ori tessellation by a quadrilateral mesh with vertices p^i . As discussed above, the mesh is generalized Miura-ori if it satisfies a planarity constraint for each face, and a developability constraint at each interior vertex. For a mesh with V vertices and $F \approx V$ faces, there are therefore $3V$ degrees of freedom and only

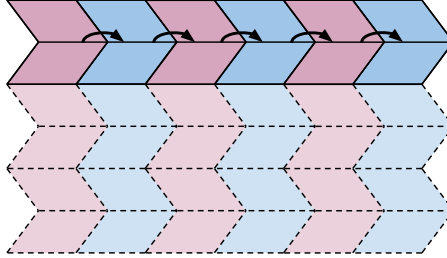


Figure S.2: Global flat-foldability Starting with the mesh in its designed configuration (some non-trivial folded state), pick a new fold angle with the same MV assignment for the first quad pair in the first column (pink, top left). Using single-vertex fold angle relations from [5] solve for fold angles for each consecutive quad pair in this column (alternating colors along the top) such that the folded width of the pair matches that of the first pair. Note that these fold angles will alternate in MV sign from pair to pair. Because the strip has constant width, the width of the folded column will also be constant through folding and the entire repeated structure will arrive at zero width simultaneously.

$V + F \approx 2V$ constraints, suggesting that the space of embedded Miura-ori tessellations is very rich; it is therefore plausible that one or more such tessellations can be found that well-approximate a given M .

Indeed, in practice for many classes of surfaces a tessellation can be found by numerical optimization. The method consists of the following steps:

1. Guess initial positions p_0^i for the vertices of the mesh based on quad mesh parameterization of M ; this guess closely approximates M but does not necessarily satisfy the planarity, developability or additional constraints.
2. Pin the corners of each unit cell guess to the quads in M , ensuring that the generalized Miura-ori surface remains close to M .
3. Solve the following constrained optimization problem to produce a developable pattern which approximates M . Note that this pinning pattern leaves at least one free node between all fixed nodes in optimization.

$$\min_{p^i} f(p^i, p_0^i) \quad s.t. \quad g_{\text{planarity}}(p^i) = 0, \quad g_{\text{develop}}(p^i) = 0$$

where the objective function f and the constraint functions are described in more detail below.

2.2.1 Initial Positions

The representation of the curved target surface is a regular, orientable quad mesh (all interior nodes have valence four and the normals of the quads are orientable). We will call this the *base mesh*. The base mesh can be obtained by discretizing the two families of curves formed by a parametrization of the target surface and forms the basis for the initial structure guess provided to the optimization routine. To construct an initial guess for the positions of all nodes in the Miura-ori structure (see Fig. S.3), we proceed by

1. populating each individual quad with 9 nodes (4 at corners, 4 at edges and 1 central),
2. displacing the edge and central nodes to construct a Miura-ori unit cell guess at each quad according to chosen orientations and local length scales, and
3. merging nodes at interior edges by averaging their positions.

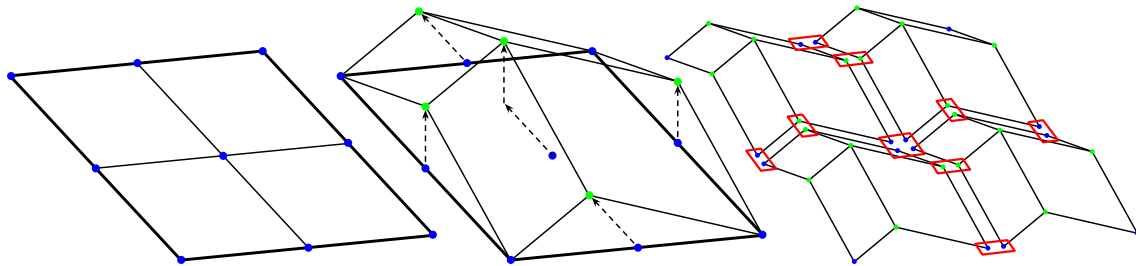


Figure S.3: **Initial positions (Left)** A single base mesh quad (bold) is initially populated with nine nodes (four corner nodes, four edge nodes given by averaging the endpoints and one central node given by averaging the four corners) which will make up a single Miura-ori unit cell (blue). **(Middle)** The central node and edge nodes in the unit cell (green) are displaced (dashed) according to the choice of pattern orientation to form a structure which “looks” like a single Miura-ori cell. **(Right)** Because each base mesh quad is converted into a single unit cell independently, we merge nodes (red) between adjacent base mesh quads to form the final mesh. For corner nodes sets (blue) this is only data structures because their positions are fixed, while for edge nodes pairs (green) we also average the two positions to produce the merged node position.

2.2.2 Fixed Nodes

The positions of the four undisplaced corner nodes in each “unit cell” are required to remain fixed throughout optimization. This ensures that the solved structure closely approximates the target surface and further flexibility in designing patterns.

2.2.3 Developability Constraints

The planarity and developability constraints can both be formulated in terms of the vertex positions p^i . For a quadrilateral face with vertices p^a, p^b, p^c, p^d oriented clockwise, planarity is equivalent to vanishing of the tetrahedral volume

$$g_{\text{planarity}} = [(p^b - p^a) \times (p^c - p^a)] \cdot (p^d - p^a).$$

Developability requires that the angles around each interior vertex sum to 2π . In other words, if the neighbors of vertex i are n_1, \dots, n_m , oriented clockwise, the developability constraint is given by

$$g_{\text{develop}} = 2\pi - \sum_{j=1}^m \angle(p^{n_j} - p^i, p^{n_{j+1}} - p^i)$$

where the angle between two vectors can be computed robustly using

$$\angle(v, w) = 2 \operatorname{atan2}(\|v \times w\|, \|v\| \|w\| + v \cdot w).$$

For the numerical optimization, the Jacobians of both constraints are required. Formulas for these derivatives can be readily computed analytically.

2.2.4 Flat-Foldability Constraints

An origami structure is called *flat-foldable* if it has a folded state in which all of its faces are coplanar (i.e. every face has moved from one plane, the initial paper, to a second plane, the flat-folded state). Consider single flat-folded vertex with four folds. One of the folds will have opposite orientation from the other three. The unique fold can be either of the two folds which *do not* touch the largest α , and will be tucked inside the other folds in the flat-folded state. In the flat-folded state, consecutive angles interior angles have opposite orientations around the vertex, and walking around this vertex is equivalent to swinging back and forth in the flat-folded state by the α values. Assuming developability, we know that

$$\alpha_1 + \alpha_2 + \alpha_3 + \alpha_4 = 2\pi.$$

Because opposite pairs of interior angles share orientation in the flat-folded state, the sums of these pair must be equal (no net change when walking around the entire vertex).

$$\alpha_1 + \alpha_3 = \alpha_2 + \alpha_4$$

From these two statements we can see that

$$\alpha_1 + \alpha_3 = \pi$$

and

$$\alpha_2 + \alpha_4 = \pi.$$

In practice, we have found that we cannot satisfy exact flat-foldability on intrinsically curved surfaces. However, we can break open the standard flat-foldability constraints into inequalities which express bounds on a flat-foldability residual. Notice that we have a single scalar at each interior vertex which represents the flat-foldability residual.

$$r_{ff} = \pi - (\alpha_1 + \alpha_3) = -(\pi - (\alpha_2 + \alpha_4))$$

Introducing a tolerance ϵ on r_{ff} in the form of a pair of inequality constraints allows the each pair of alternating angles at an interior vertex to sum to a value within ϵ of π .

$$g_{\text{flat-foldability}}(p^i) = \pm r_{ff} - \epsilon \leq 0$$

In the limit $\epsilon \rightarrow 0$ these inequalities reduce to the standard equality Kawasaki condition.

2.2.5 Special Cases

- Rotational Symmetry

For surfaces with rotational symmetry we enforce developability constraints over a symmetric strip using periodic boundary conditions. The symmetric strip can then be used to reconstruct the full developable Miura-ori structure. This strategy is particularly useful when analyzing the asymptotic behavior of solved patterns over magnitudes of order changes in pattern resolution, as the computational demands are linear in strip resolution but the size of the solved pattern grows quadratically with strip resolution. We employed this strategy for the sphere, hyperboloid and all mixed curvature examples.

- Triangulated Pattern

For some examples, the developability constraint residuals fail to vanish completely. Typically these non-zero values are on the order of at most $1e - 6$. These residuals can still introduce error in the layout process, however, so in these cases we employ a second phase of optimization:

- introduce additional degrees of freedom in the optimization by dropping the quad planarity constraint,
- triangulate the pattern so that each interior node has six incident edges (and therefore six incident interior angles) and
- solve $g_{\text{develop}} = 0$ over six angles rather than four at each interior node.

We only found need to employ triangulation on surfaces with rotational symmetry, and we report the relevant residuals associated with both optimization phases with each example.

- Normalized Quad Planarity

Because the quad planarity constraint $g_{\text{planarity}}(p^i) = 0$ is just the volume of the quad, it scales as L^3 with the length L of the pattern edges. For most examples we are able to solve these constraints to arbitrary precision and the scaling is irrelevant. However, for the hyperboloid we compute patterns over two orders of magnitude of pattern resolution, so the scaling of $g_{\text{planarity}}$ becomes relevant: more highly resolved patterns can more easily satisfy quad planarity by virtue of their smaller length scales. To address this, we solve a normalized version of quad planarity:

$$g_{\text{planarity-norm}} = \frac{g_{\text{planarity}}^j}{L_j^3} = 0,$$

where L_j is a length scale associated with the initial geometry of the j^{th} quad. We choose L_j to be the mean of the four initial side lengths of quad j .

2.2.6 Objective Function

The objective function minimizes changes in the lengths of pattern edges and cross edges (see Fig. fig:objective) of the initial guess. Edge i with current length L^i and initial length L_0^i contributes

$$E_i = \frac{1}{2L_0^i}(L^i - L_0^i)^2.$$

Because this energy is not balanced against other terms we neglect a stiffness prefactor. The objective function is zero at the beginning of each run and $\sum_{i=1}^M E_i$ for a structure of M total edges (pattern and cross) thereafter. The purpose of the objective function is to preserve the initial user-provided positions as closely as possible during optimization (E_i has no physical significance).

2.2.7 Numerical Optimization Approach

We implement the numerical optimization in Matlab using the Interior Point algorithm of `fmincon`. Fixed nodes can be implemented either as linear (which require no Jacobian) or simply by leaving these variables out of p^i . We provide analytic Jacobians for planarity and developability constraints (non-linear equality) and flat-foldability constraints (non-linear inequality). Successful optimizations typically find minima and satisfy constraints by a maximum residual of 1e-10 within several hundred iterations.

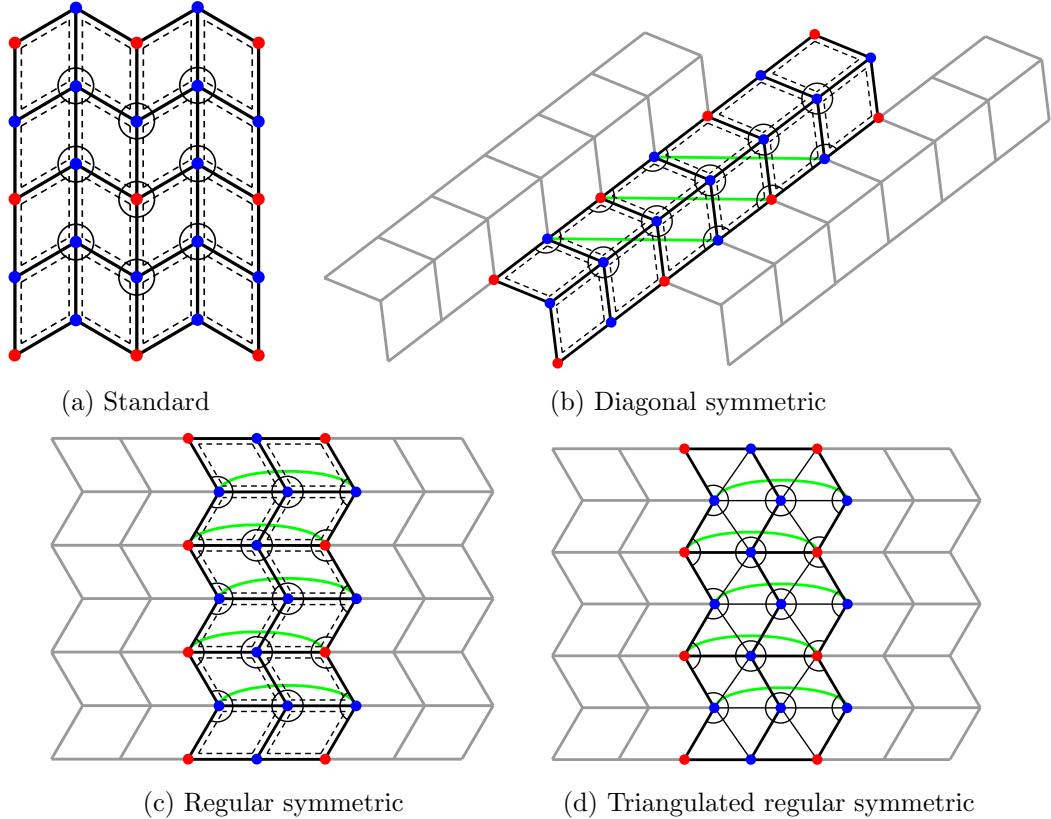


Figure S.4: **Constraint patterns** Blue nodes: free, red nodes: fixed, dashed quads: $g_{\text{planarity}}$, open circles: g_{develop} and $g_{\text{flat-foldability}}$, green arcs: rotational symmetry pairs

3 Examples

See Fig. S.6 for additional structures and patterns not presented in the main text.

4 Foldability

Note that satisfying $g_{\text{planarity}} = 0$ and $g_{\text{develop}} = 0$ guarantees the existence of only two states (three counting the mirror symmetric configuration obtained by flipping all MV assignments) of the curved Miura-ori structure: a single folded configuration in R^3 and a developed pattern in R^2 . The existence of other folded states of the pattern and, in particular, the existence of a continuous, isometric global motion from flat to solved states (i.e. a *rigid folding*) are also of interest. The existence of a rigid folding of a quad-based

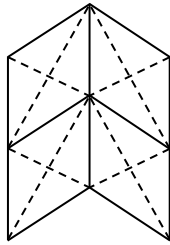


Figure S.5: **Objective function** The objective function is based on linear springs at the pattern edges (solid) and cross edges of each quad (dashed) in the initial configuration.

generalized Miura-ori structure would necessarily have a single DOF and would therefore constitute a *mechanism*, an obviously desirable property for engineering applications.

Tachi [1] finds that a generic quadrilateral structure is rigid-foldable if it is

- everywhere locally flat-foldable (satisfies the Kawasaki condition) and
- a non-trivial configuration (neither flat nor flat-folded states) of the structure exists.

These are sufficient conditions for the existence of a rigid folding motion from flat to flat-folded, passing through the non-trivial configuration. This means that *if* we can solve for a folded state of a curved Miura-ori structure with flat-foldability enforced exactly at all interior nodes, we are guaranteed a rigid-foldable structure with one DOF. Such a structure would be able to fold from flat to its solved state (non-trivial configuration) and *past* its solved state to a flat-folded state (all faces are coplanar and all fold angles are $\pm\pi$).

All generalized cylinders examples we produce are flat-foldable and therefore rigid-foldable by geometric construction. In the case of generic surfaces, however, we are unable to find exactly flat-foldable solutions. In order to fold generic material structures then, we expect geometric frustration to induce bending in quad faces in intermediate folding states. We characterize the geometric frustration in the folding process with a simple mechanical simulation, and show that even if an exactly flat-foldable structure cannot be found, optimizing with bounds on the flat-foldability residual mitigates this frustration. Recall the inequality constraint $g_{\text{flat-foldability}}$ from Section 2.2.4. Because of the relationship between flat-foldability and rigid-foldability laid out in [1], we expect that as we tighten the ϵ bounds on $g_{\text{flat-foldability}}$ the solved structure approaches rigid-foldability as well.

Keep in mind that the structures discussed so far in this section are assumed to be quad-based with all valence 4 interior nodes, and that rigid-foldability would preserve the planarity of quads between flat and folded states. Instead we divide each quad into two triangles (effectively dropping quad planarity and adding extra DOFs to the structure) and in practice are able to rigidly fold these subdivided structures from flat to solved (folded) states by allowing each quad to bend along the newly introduced crease in intermediate

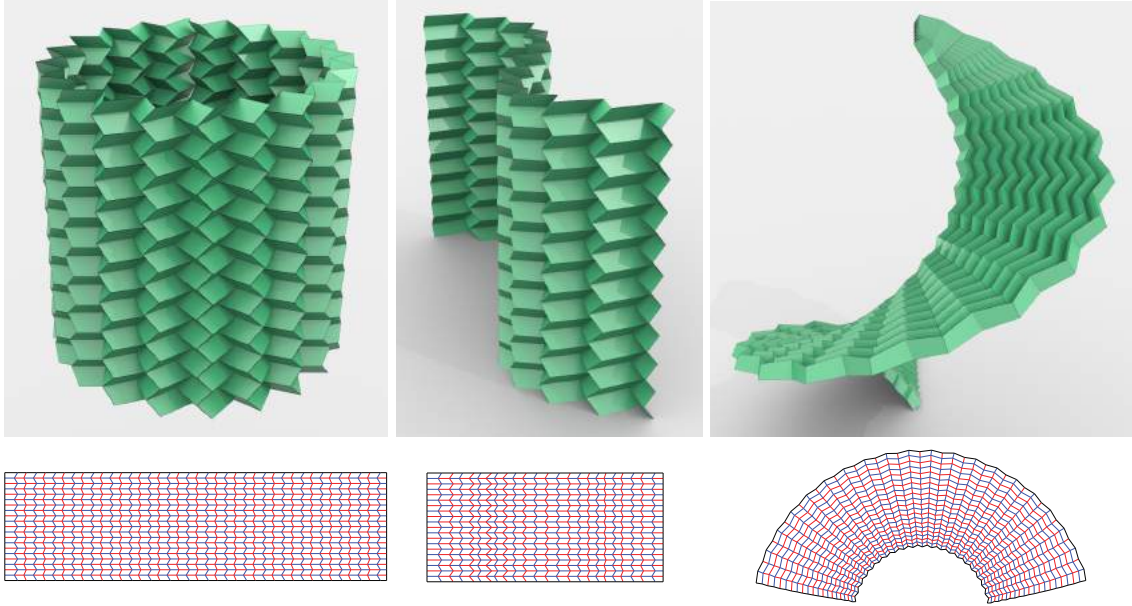


Figure S.6: **Additional results** (**Left**) Geometric construction: cylinder (**Middle**) Geometric construction: sinusoidal wave (**Right**) Numerical method: helicoid

folding states. This folding motion is a rigid folding, but does not constitute a mechanism because of the additional DOFs. We compute these rigid folding motions using a simple mechanical simulation detailed below.

4.1 Simulation Method

Using the hyperbolic paraboloid pattern (hypar), we begin by choosing a single fold near the center of the pattern (see Fig. S.7). This fold is then constrained to incrementally changing fold angles from solved to flat in simulation, the actuation of which propagates throughout the structure by the equilibration of bending energies in the quads, effectively unfolding the pattern mechanically. All edge lengths remain constant (enforced by non-linear constants) during simulation, and thus the computed folding motion is rigid.

Stating this procedure formally, we solve the following optimization problem

$$\min_{p^i} f(p^i, p_0^i) \quad s.t. \quad g_{\text{edges}}(p^i) = 0, \quad g_{\text{fold}}(p^i) = 0,$$

where

$$f_j(p^i, p_0^i) = \frac{1}{2} k_j \theta_j^2$$

is the sum of all bending energies in the quad faces,

$$g_{\text{edges}}(p^i) = \|e_k\| - L_k$$

is the edge length constraint, and is enforced at all edges with initial lengths L_k in the triangulated pattern, and

$$g_{\text{fold}}(p^i) = \theta - \theta_{\text{pinch}}$$

is the pinched fold angle constraint, enforced at a single fold in the interior of the pattern with θ its fold angle and θ_{pinch} the prescribed fold angle. Each incremental optimization takes the equilibrium node positions at the previous intermediate folding configuration as p_0^i .

Note that the only bending energies present in f are all *within* the quad faces. No fold angle, which resides at an interior edge between two adjacent quads, contributes to the objective function. And with the exception of the pinched fold, all fold angles are unconstrained and can move freely during optimization. Therefore, if the quad-based Miura-ori structures we solve for were indeed rigid-foldable without additional DOFs from triangulation, we would expect to find a zero-energy configuration of the mesh at every intermediate state between flat and folded. Taken together these configurations would constitute a rigid folding of the quad mesh. We do not, however, observe such intermediate states in any folding simulations and therefore conclude that these structures can only be rigidly folded with the additional DOFs.

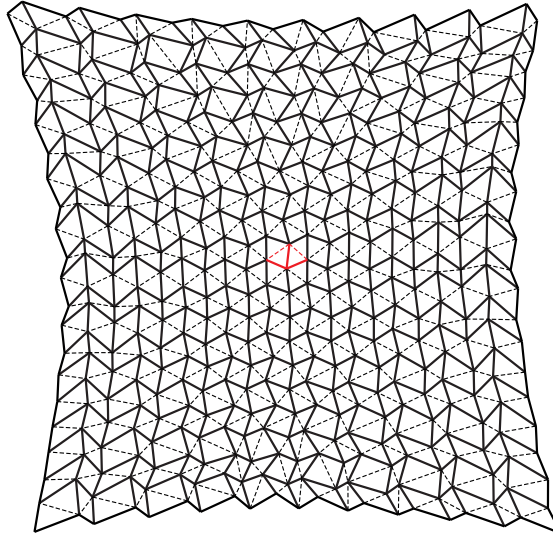


Figure S.7: Triangulation of quad-based hypar pattern Solid lines: original patterns quads, dashed lines: Delaunay subdivision of quads, red lines: “pinched” fold

4.2 Structural Mechanics of Origami

To compare our simulation results with real material structures, we connect the bending stiffnesses assigned in simulation to the Young's modulus and bending stiffness of the material/structure.

Our bending model is based on adjacent triangles in each flat quad, so we need to connect the folding of a triangle pair to the uniform bending of a linearly elastic material piece of the same area and thickness.

Consider a triangle pair with areas A_1 and A_2 and shared edge length L . This pair has the same area as a rectangle of width $w = L/2$ and length $a = 2(A_1 + A_2)/L$. If we bend this rectangle uniformly along its length into a circular arc also of length a (see Fig. S.8a and Fig. S.8b), we observe that the radius of curvature of this arc is $R = a/\theta$, where θ is the fold angle (i.e. exterior to the dihedral angle between the two faces). This comes from the fact that $\alpha/2 + (\pi - \theta)/2 + \pi/2 = \pi$.

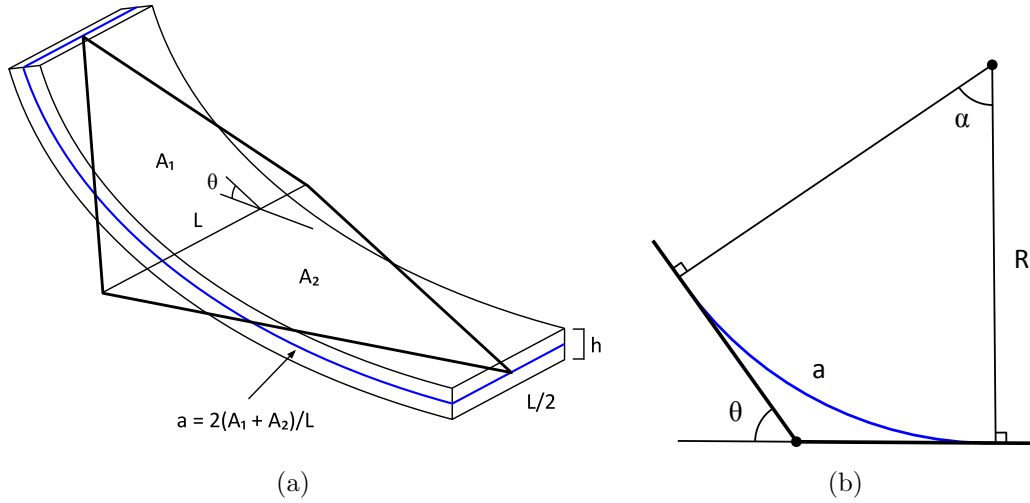


Figure S.8: **Bending stiffness** (a) Bending stiffness triangle pair with inscribed arc (b) Profile of bent triangle pair

Now that we can connect the geometry of bending of two triangles and a rectangular volume, we can derive a bending stiffness by equating the bending energies.

A uniformly bent sheet with length a , constant thickness h , second moment of inertia I and Young's modulus E has strain energy due to stress along its length

$$U_b^\theta = \frac{1}{2}EI\kappa^2a,$$

where κ is the curvature of the sheet's mid-plane. We can compute $I = \int_A z^2 dA$ for the bent sheet where A is the cross-sectional area, z is in the direction of the thickness and $L/2$ is the width.

$$I = \frac{1}{24} L h^3$$

Substituting I and $\kappa = 1/R$ gives

$$U_b^\theta = \frac{1}{48} \frac{ELh^3a}{R^2}.$$

Equating this to the discrete bending energy model f_j above gives

$$\frac{1}{2} k_j \theta^2 = \frac{1}{48} \frac{ELh^3a}{R^2},$$

where all parameters now belong to the two triangles inside quad j . Substituting $R = a/\theta$ gives

$$\frac{1}{2} k_j \theta^2 = \frac{1}{48} \frac{ELh^3}{a} \theta^2.$$

Substituting $a = 2(A_1 + A_2)/L$ gives our final bending stiffness k .

$$k_j = \frac{1}{48} \left(\frac{L^2}{A_1 + A_2} \right) Eh^3$$

For results presented in the main text we use $E = 10^9 \text{ N/m}^2$ and $h = 10^{-4} \text{ m}$, reasonable values of paper-like material, to compute k_j and we non-dimensionalize the total bending energies by the largest observed bending energy in a single material quad across all simulations, $9.764 \times 10^{-8} \text{ J}$.

4.3 Experimental measurement of Hypar stiffness

As discussed earlier, our simulations show that a larger flat-foldability residual leads to a higher energetic barrier between the flat and folded configurations. This bistability is likely a desired property in deployable structures that need to be (at least) locally stable. To verify this trend experimentally, we measure the stiffness of a pair of calculated hypars with different flat-foldability residuals. After laser-cutting the tessellations onto a sheet of paper, we fold these structures and attach inextensible thread and paper paddles to one unit cell close to the boundary of the folded structure. We then conduct a simple force extension experiment using an Instron (see Fig. S.9) over a strain range of 0.2 using the following protocol: extend the structure at 5 mm/s until the maximum nominal strain is reached, and then reverse the process till the force goes back to zero. We then repeat the experiment two more times. We find that the first “run-in” experiment is different

and reflects the irreversible deformations associated with the virgin origami structure, but eventually the force-extension plot settles onto a steady curve. We see that the curve for the hypar with the larger flat-foldability residual is stiffer, and underscores the change in global mechanical response of the structure by a modification of local geometry, as predicted by our simulations.

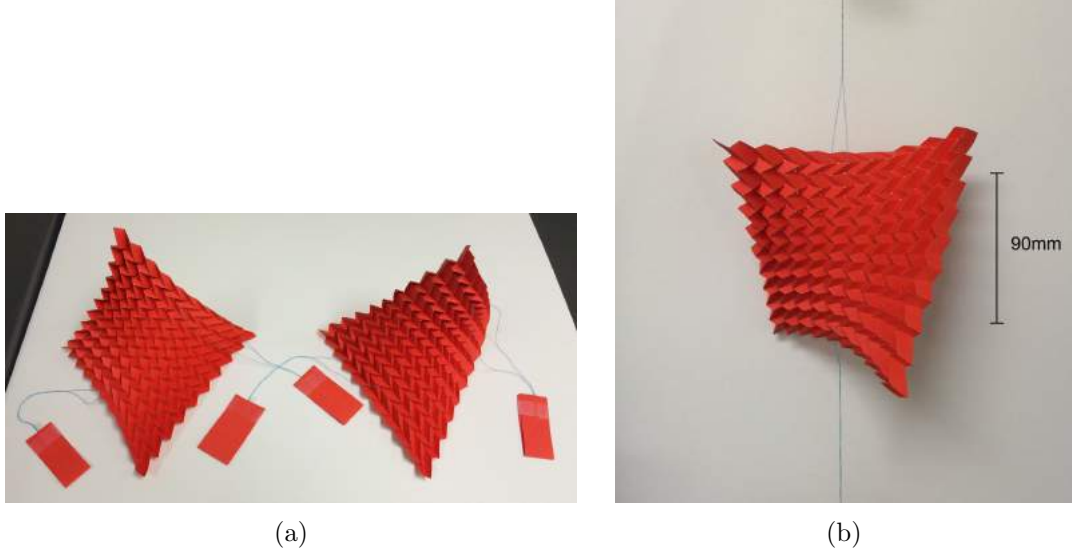


Figure S.9: **Stiffness experiment** (a) Structures corresponding to patterns $\epsilon_{ff} = \epsilon_0, \epsilon_0/10$ (b) Loading a hypar in the Instron

5 Accuracy vs. Effort: Hyperboloid of a Single Sheet

In addition to providing examples of origami surfaces with a variety of curvatures, we are also interested in optimizing the trade-off between approximation accuracy and pattern resolution. It is natural to expect that as we increase the resolution of generalized Miura-ori surface, we would be able to approximate its target surface more accurately. However, it is also easy to imagine a scenario, in particular in real-world applications, in which increased resolution incurs some fabrication cost (time and complexity). It is also unknown whether significantly increasing resolution and accuracy would incur an additional material cost, i.e. the limiting behavior of the areas of increasingly resolved generalized Miura-ori surfaces. We use simple numerical experiments fitting the hyperboloid of one sheet to provide insight into these questions, illustrating the trade-off between accuracy and resolution.

The hyperboloid of one sheet has a number of properties that make it a natural setting for investigating these questions computationally.

- Negative Gauss curvature: As we have observed, negatively curved surfaces are more natural settings for fitting generalized Miura-ori surfaces. We expect fast, accurate convergence on the hyperboloid without having to resort to optimization setups with additional DOFs.
- Rotational symmetry: We can reduce the entire surface to a single symmetric strip, which significantly reduces the computational demands of increased surface resolution in optimization. In particular, the size of the dense Jacobian provided to `fmincon` is quadratic in the number of unit cells per symmetric strip, rather than quartic, which would be the case without rotational symmetry.
- Ruled surface: Conveniently, the hyperboloid has *two* symmetric families of rulings. Taken together, these families form a natural base mesh for optimization, so the choice of symmetric strip is not arbitrary, but rather given by the geometry of the hyperboloid and the desired resolution.

5.1 Base Mesh: Diagonal, Rotationally Symmetric Strip

A hyperboloid of one sheet with waist radius a and rotational symmetry about the z -axis is given implicitly by

$$\frac{x^2}{a^2} + \frac{y^2}{a^2} - \frac{z^2}{c^2} = 1.$$

Choosing $a = \sqrt{2}/2$ and $c = 1$, simply for aesthetics, this surface can be parameterized by

$$\begin{aligned} x(t, v) &= \cos t + v(\pm \sin t - \cos t) \\ y(t, v) &= \sin t + v(\mp \cos t - \sin t) \\ z(t, v) &= 2(v - \frac{1}{2}). \end{aligned}$$

We will focus on the surface patch given by $t \in [0, 2\pi], v \in [0, 1]$. The sign change in the parameterization gives two families of rulings (see Fig. S.10). A single ruling, which runs diagonally on the surface of the hyperboloid, can be obtained by holding t constant and varying v . This parameterization is convenient because at $v = 0$ we have the bottom circular boundary of the surface patch of interest.

By sampling the rulings families over an even number of uniform intervals along the bottom circle we can construct the diagonal grid seen in Fig. S.10. Furthermore, if we divide the bottom circle into $2(n + 1)$ arcs and extend rulings from the endpoints of these arcs, each diagonal, rotationally symmetric strip in the base mesh will have n quads (giving

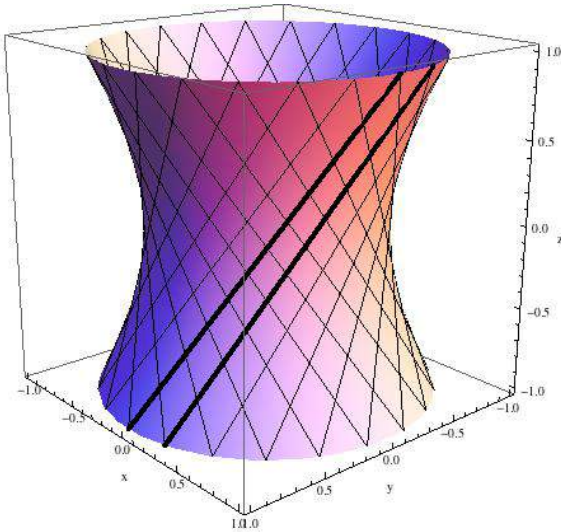


Figure S.10: Hyperboloid of one sheet The two families of rulings (black) intersect to form a natural base mesh. Here we have chosen 10 quads in each diagonal, rotationally symmetric strip. Two consecutive rulings (bold black) mark the periodic boundaries of a symmetric strip.

$2n(n + 1)$ quads over the whole hyperboloid). The symmetry between rulings families also guarantees that the left and right nodes in each quad are themselves rotationally symmetric. Recall that all of the nodes in the base mesh remain fixed during optimization, allowing us to exploit the underlying symmetry of the base mesh via the constraint pattern in Fig. S.4b.

5.2 Examples

We produce numerical results for hyperboloids with 10 to 100 (intervals of 10) and 100 to 1000 (intervals of 100) unit cells per symmetric strip for a total of 19 generalized Miura-ori structures over two orders of magnitude in strip resolution (see Fig. S.11 and Fig. S.12). We use diagonally-symmetric developability constraints and area normalization in quad constraints (see Section 2.2.5) to ensure scale-independent satisfaction of convergence tolerances at small length scales ($g_{\text{planarity-norm}} = 0$ and $g_{\text{develop}} = 0$ are both satisfied within tolerances of 10^{-10}).

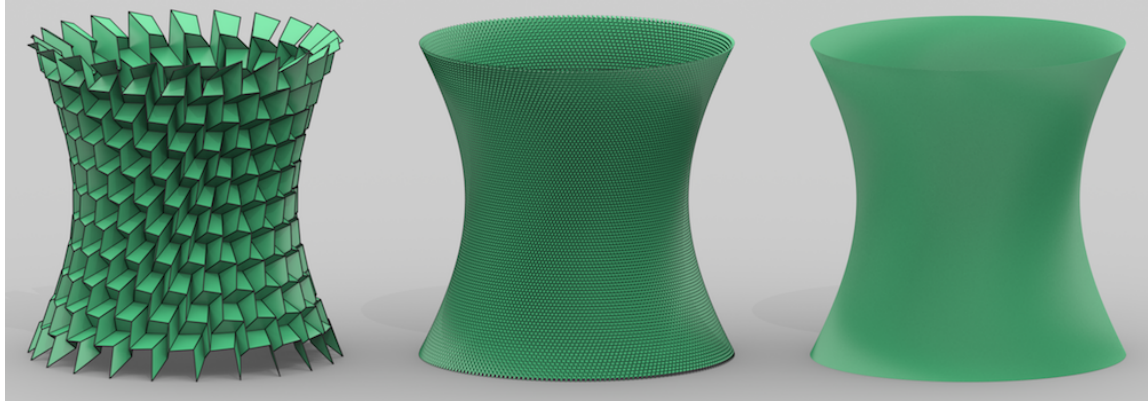


Figure S.11: **Generalized Miura-ori hyperboloids (Left to Right)** 10, 100 and 1000 unit cells per symmetric strip

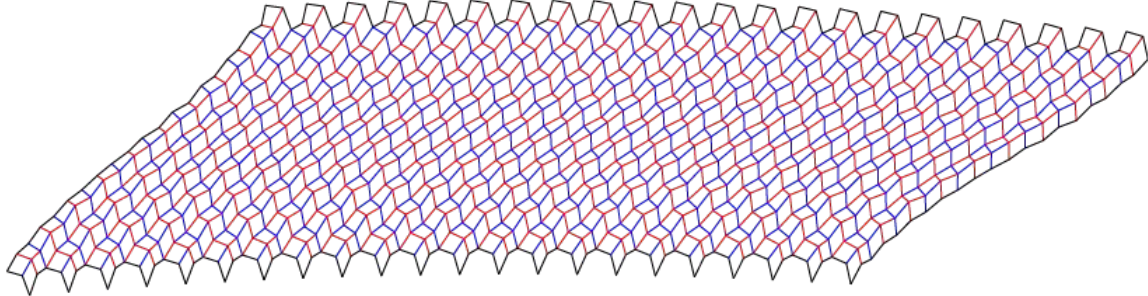


Figure S.12: **Generalized Miura-ori hyperboloid development** 10 unit cells per symmetric strip

5.3 Computing the Hausdorff Distance

The Hausdorff distance d_H is defined as the maximal distance between the points in one set and their closest points in another set, as viewed from both sets. More formally, for two sets M and S , d_H is given by

$$\begin{aligned} d_H(M, S) &= \max[d(M, S), d(S, M)] \\ d(M, S) &= \max[d(x, B)], \quad \forall x \in M \\ d(x, S) &= \min[d(x, y)], \quad \forall y \in S. \end{aligned}$$

Denoting the Miura-ori hyperboloid M and the target hyperboloid S , we compute $d(M, S)$ between each Miura-ori hyperboloid and the target surface computationally, as no analytic

expression of distance from a point in space to the hyperboloid surface exists, and set this equal to $d_H(M, S)$. Because the target hyperboloid is a continuous surface consisting of infinite points we cannot compute $d(S, M)$, but we note that in this particular case $d_H(M, S) = d(M, S)$, up to some error bound, as proved next.

Let M be a quadrilateral mesh (possibly non-developable with non-planar faces) and S a compact smooth Riemannian manifold (possibly with boundary) embedded in \mathbb{R}^3 . For each vertex v_i of M , let \tilde{v}_i be its orthogonal projection onto S (we assume that all points of M are close enough to S , relative to the curvature of S , so that their projections are unique). Let $\delta = \max_i \|v_i - \tilde{v}_i\|$ and

$$\epsilon = \max_{p \in S} \min_i g(p, \tilde{v}_i)$$

where $g(p, q)$ is geodesic distance on S ; in other words, ϵ^{-1} bounds how densely the projected mesh points sample the surface. Finally, let

$$\eta = \max_{i \sim j} g(\tilde{v}_i, \tilde{v}_j),$$

where the maximum is taken over all projections of neighboring vertices on M . Then the Hausdorff distance between S and M satisfies

$$d_H(S, M) \leq 2\delta + \max(\eta/2, \epsilon).$$

First, notice that if v_i and v_j are neighboring vertices, $\|v_i - v_j\| \leq \eta + 2\delta$. Let p be a point on M . By the triangle inequality, if v is the closest vertex of M to p , then $\|p - v\| \leq \eta/2 + \delta$, and $\|p - \tilde{v}\| \leq \eta/2 + 2\delta$, so

$$d(M, S) \leq \eta/2 + 2\delta.$$

Next, clearly $d(S, M) \leq \epsilon + \delta$, proving the theorem.

Notice that displacing the vertex v_i in the direction normal to the surface changes δ , but not the other bounds, therefore finding such normal displacements that minimize δ also minimizes the above bound on Hausdorff distance. When the points v_i are allowed to slide tangentially (which may be required in order to enforce the Miura constraints on M) minimizing δ remains a good heuristic, as for example when fixing some of the points at $v_i = \tilde{v}_i$ to bound increases in η and ϵ .

To compute $d(M, S)$ for the hyperboloid, consider a point

$$p = (x_p, y_p, z_p)$$

in R^3 and a surface parameterization

$$S(t, v) = (x_s(t, v), y_s(t, v), z_s(t, v)).$$

The distance D between p and a point on S is given by

$$D(t, v) = \sqrt{(x_p - x_s(t, v))^2 + (y_p - y_s(t, v))^2 + (z_p - z_s(t, v))^2}.$$

For each point in the generalized Miura-ori hyperboloid we can identify its closest point on the target hyperboloid S by minimizing D^2 with respect to t and v , which we implement by providing analytic Jacobians to Matlab's `fminunc`. Computing d_H for each optimization result is straightforward once these correspondences are established.

5.4 Accuracy/Effort Trade-Off

We construct a cost function from weighted, linear combinations of the data sets d_H (Hausdorff distance between Miura-ori and target hyperboloids) and N (total number of unit cells in the Miura-ori hyperboloid). We normalize each set by its largest value to produce

$$\hat{d}_H = \frac{d_H}{\|d_H\|_\infty} \text{ and } \hat{N} = \frac{N}{\|N\|_\infty}.$$

The cost function C is a weighted sum of \hat{d}_H and \hat{N} (weights w_d and w_N , respectively).

$$C = w_d \hat{d}_H + w_N \hat{N}$$

By tuning the ratio w_N/w_d we can produce cost functions with different minima and therefore different optimal Miura-ori hyperboloids.

5.5 Area Convergence

Because all quads in the Miura-ori hyperboloids are planar, we simply sum their areas to compute the total area of a structure. These areas converge in the limit of strip resolution $n \rightarrow \infty$ and the area asymptote A_0 for the Miura-ori hyperboloids is ~ 24.13 , whereas the actual area of the smooth hyperbolic target patch is ~ 10.77 . This factor of ~ 2.24 difference could be likely be reduced with different initial position parameters, but we expect any reduction to be minimal. Our convergent Miura-ori approximation constitutes an isometric *wrapping* of the hyperboloid as defined in [6].

For comparison, we can construct an alternative developable approximation of the same hyperboloid using a single family of rulings as shown in Fig. S.13 and Fig.S.14. In this construction, a symmetric strip consists of two triangles generated by two consecutive

rulings and a diagonal between them. To first order in t , the area of these two triangles (a symmetric strip), is

$$t\sqrt{5 - t + \frac{5}{4}t^2}, t = \frac{2\pi}{2(n+1)}.$$

Again, n is the number of quads in a single symmetric strip and $2(n+1)$ is the total number of strips, borrowed from the Miura-ori construction for comparison. From this it is easy to see that the alternative construction has an total area approaching $2\pi\sqrt{5} \approx 14.05$ in the limit $n \rightarrow \infty$, for a ratio of ~ 1.30 . While this singly-corrugated construction has a limiting area which more closely approximates the hyperboloid, the convergence of this area still follows the length scale of the discretization and such specialized constructions only exist for special target surfaces, such as ruled surfaces. Future work could classify these limiting area ratios for different origami tessellations and different surface types.

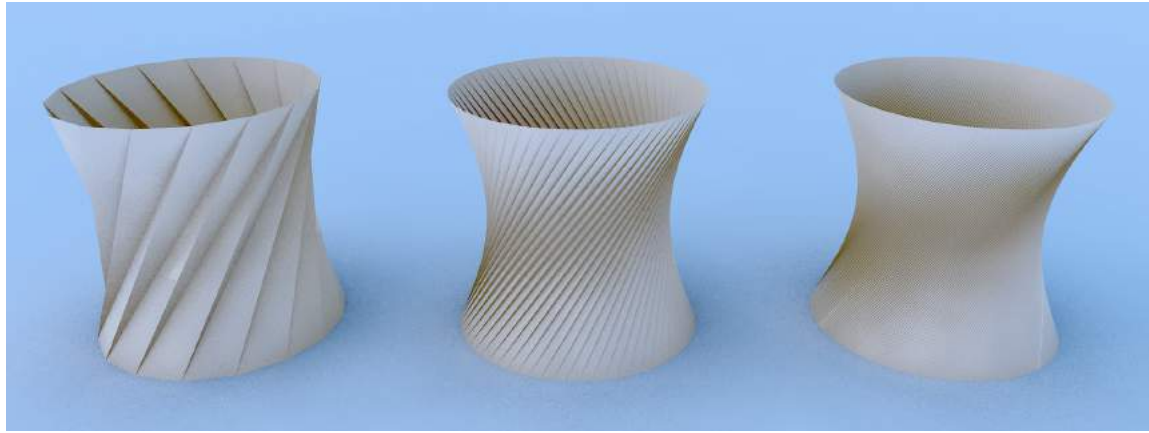


Figure S.13: Hyperboloid of one sheet, alternative construction Using a single family of rulings and with pairs of triangles between consecutive rulings to generate a developable construction of the hyperboloid.

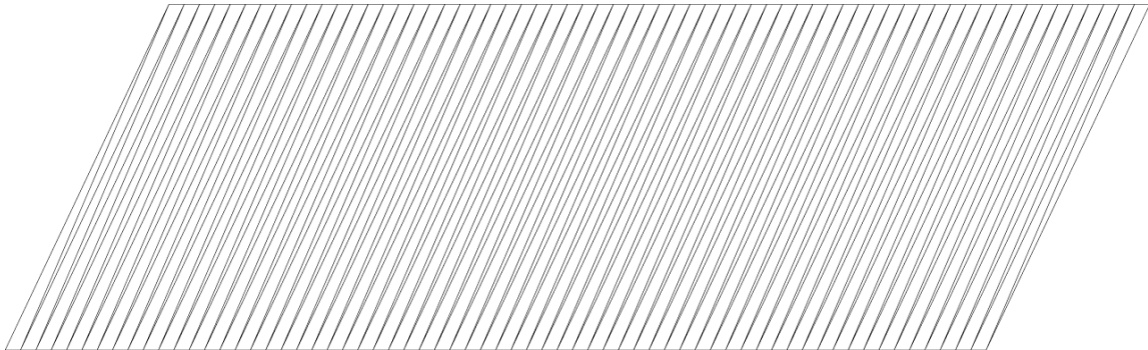


Figure S.14: **Hyperboloid of one sheet, alternative construction, development**

References

- [1] T. Tachi, “Generalization of rigid foldable quadrilateral mesh origami,” *Proceedings of the International Association for Shell and Spatial Structures (IASS) Symposium* (2009)
- [2] X. Zhou, H. Wang, Z. You, “Design of three-dimensional origami structures based on vertex approach,” *Proceedings of the Royal Society A* **471** 2181 (2015)
- [3] M. W. Bern, B. Hayes, “The Complexity of Flat Origami,” *Proceedings of the Seventh Annual (ACM-SIAM) Symposium on Discrete Algorithms*, Atlanta, GA, pp. 175-183 (1996)
- [4] T. Kawasaki, “On the Relation Between Mountain-Creases and Valley-Creases of a Flat Origami,” *Proceedings of the 1st International Meeting on Origami Science and Technology* (Ed. H. Huzita), Ferrara, Italy, pp. 229-237 (1989)
- [5] D. A. Huffman, “Curvature and Creases: A Primer on Paper,” *IEEE Transactions on Computers* **10** 25, pp. 1010-1019 (1976)
- [6] E. D. Demaine, M. L. Demaine, J. Iacono, S. Langerman, “Wrapping the Mozartkugel,” *Abstracts from the 24th European Workshop on Computational Geometry (EuroCG 2007)*, Graz, Austria, pp. 14-17 (2007)